This ESI replaces the original version published on 15 Mar 2024.

Supporting Information

Liquid-Templated Graphene Aerogel Electromagnetic Traps

Seyyed Alireza Hashemi [a #], *Ahmadreza Ghaffarkhah* [a, b #], *Farhad Ahmadijokani* [a, b], *Hatef Yousefian* [a], *Sameer E. Mhatre* [b], *Anna Sinelshchikova* [c], *Gabriel Banvillet* [b], *Milad Kamkar* [d], *Orlando J. Rojas* [b], *Stefan Wuttke* [c, e], *and Mohammad Arjmand* [a *]

[a] Nanomaterials and Polymer Nanocomposites Laboratory, School of Engineering, University of British Columbia, Kelowna, BC, V1V 1V7, Canada

[b] Bioproducts Institute, Department of Chemical & Biological Engineering, Department of Chemistry and Department of Wood Science, 2360 East Mall, The University of British Columbia, Vancouver, BC V6T 1Z3, Canada

[c] Basque Centre for Materials, Applications & Nanostructures (BCMaterials), Bld. Martina Casiano, 3rd. Floor UPV/EHU Science Park Barrio Sarriena s/n, Leioa, 48940 Spain

[d] Department of Chemical Engineering, Waterloo Institute for Nanotechnology, University of Waterloo, 200 University Avenue West, Waterloo, Ontario N2L 3G1, Canada

[e] Ikerbasque, Basque Foundation for Science, Bilbao, 48009 Spain

[#] These authors equally contributed to the preparation of this assay

***Corresponding Author:** mohammad.arjmand@ubc.ca

Table of Contents

1. Detailed synthesis protocols

1.1. Synthesis of graphene oxide (GO)

The synthesis of GO was carried out through the exfoliation of graphite via our previously reported protocols.[1, 2] Briefly, a 9:1 volume ratio of sulfuric acid (H_2SO_4) and ortho-phosphoric acid (H_3PO_4) (360 mL:40 mL) were mixed for 10 min at 350 rpm, followed by the addition of 3 g graphite. The mixture was stirred for 30 min till full infiltration of H_2SO_4 between galleries, forming an H_2SO_4:H_3PO_4-graphite intercalant compound. Next, the reaction temperature was declined by an ice bath (~5 °C), and 18 g potassium permanganate ($KMnO_4$) was slightly added to the mixture. The reaction temperature was thence elevated slightly to 55 °C using an oil bath, leading to the oxidation of graphite flakes, viz., the formation of pristine graphite oxide. The reaction was kept stirring at 55 °C for 18 h, followed by termination with a mixture of H_2O:H_2O_2 (800 mL:5 mL). In this step, the weakened van der Waals forces between galleries of graphite oxide flakes were terminated, forming exfoliated GO. The mixture was stirred for 2 h and thence applied to purification and separation steps. For purification, the GO was separated from the acidic medium through centrifugation at 11000 rpm, followed by sequence washing and centrifugation with DI water, 30 vol% HCl solution, ethanol, and again DI water. The purified GO suspension was bath sonicated for 1 h, and thence concentrated through centrifugation at 11000 rpm to reach a paste of GO with a concentration of 10 mg mL^{-1}. The concentrated paste was kept in a sealed container at ambient temperature till further use.

1.2. Synthesis of cellulose nanofiber (CNF)

The synthesis of cellulose nanofibers and their subsequent TEMPO-mediated oxidation process was performed according to our previous study.[1] In this regard, 230 g of refined bleached

Eucalyptus kraft pulp was mixed with a repulper in 11.5 L DI water two times. This process was performed via a valley beater till obtaining a CSF of 350, reaching a pulp-DI water mixture with concertation of 1.5 wt%. Next, 0.24 g TEMPO and 1.545 g NaBr were mixed in 150 mL DI water to get a homogenous suspension. At the same time, a 42.945 g NaCIO (13%) solution was poured into a beaker, and the pH was set to 10 via 3 M HCl. The pulp-DI water suspension was thence poured into a large container and mixed at room temperature (RT) at 200 rpm. In the next step, the NaBr/TEMPO mixture was added to pulp-DI water suspension and mixed for 3 min, followed by a slight and dropwise addition of pH-adjusted NaCIO solution to the blend. The suspension volume was thence increased to 3L by adding more deionized water. Using 3M NaOH, the pH of the blend was increased to 10 till no more change in the pH occurred. This implies full consumption of the NaCIO in the reaction, and no further carboxylic functional groups were formed. The pH was declined to 7 via adding 3 M HCl, and the mixture was centrifuged at 8000 rpm for 5 min until reaching a supernatant with a conductivity of 5 $\mu S\ cm^{-1}$. The as-prepared CNF paste was then stored in a refrigerator till further use. Full characterization of the generated Tempo-oxidized CNF can be seen in our previous study.[1]

2. Electromagnetic shielding measurements

The electromagnetic (EM) shielding characteristic of the generated aerogels was analyzed via a two-port vector network analyzer (VNA) (P9374A Keysight) within the X-band frequency range (8.2-12.4 GHz) using a WR90 waveguide. To this end, the aerogels were attached to an offset short and sandwiched between waveguide adaptors. The samples were then exposed to EM waves in the X-band frequency range, and their complex scattering (S-) parameters were collected. Then, the scattering parameters were used to calculate reflectance (R), transmittance (T), and absorbance (A) using the following equations:

$$R = |S_{11}{}^2| = |S_{22}{}^2| \quad (1)$$

$$T = |S_{21}{}^2| = |S_{12}{}^2| \quad (2)$$

$$A = 1 - R - T \quad (3)$$

where S_{11} and S_{22} denote the reflected EM waves to ports 1 and 2, while S_{21} and S_{12} are attributed to the transmitted EM waves to ports 1 and 2, respectively. The shielding coefficients were used to measure the reflection loss (SE_R), absorption loss (SE_A), and total shielding effectiveness (SE_T) according to the following formulations:

$$SE_R = 10 \log \left(\frac{1}{1-R}\right) \quad (4)$$

$$SE_A = 10 \log \left(\frac{1-R}{T}\right) \quad (5)$$

$$SE_T = SE_A + SE_R \quad (6)$$

The specific shielding effectiveness (SSE/t) of the aerogel samples was measured as follows:

$$SSE/t = \frac{SE_T}{\rho * t} \quad (7)$$

in which ρ and t are the density and thickness of the sample in g cm^{-3} and cm, respectively. The anti-reflection performance of the aerogels was analyzed with the same procedure while one side of the aerogels (the side opposite to the incident wave port) was covered with metallic substrates, including aluminum (Al) foil (thickness:15 μm), carbon-coated Al (C-Al) foil (thickness:15 μm), copper (Cu) foil (thickness:10 μm), Cu tape (thickness:50 μm), titanium (Ti) foil (thickness:20 μm), Ti mesh (thickness:426 μm), or Zn foil (thickness:106 μm).

3. Nanomaterials characterization

In this section, the developed nanomaterials were characterized via different techniques to confirm their successful synthesis with the required features. Figure S1 (a) showcases the FTIR spectrum of GO. As depicted, the GO was synthesized with typical functional groups of the acidic exfoliation methods, including hydroxyl functional groups (-OH) (3403 cm^{-1}), carbonyl (C=O) (1736 cm^{-1}), unoxidized C=C double bond carbon atoms (1632 cm^{-1}), C-OH (1358 cm^{-1}), C-O-C (1225 cm^{-1}), and C-O (1083 cm^{-1}). [1, 2] Additionally, the X-ray diffractogram of the GO (Figure S1 (b)) showed a 2Θ peak of 11° corresponding to the interlayer spacing (d-spacing) of 8.02 Å and (001) crystalline plane of GO. This increase in the d-spacing compared with the graphite (3.4 Å) is due to the creation of oxygen domains on the surface of the GO.[3, 4] Following other analyses, the micro-Raman spectroscopy (Figure S1 (c)) also showed the successful formation of GO by revealing two well-defined characteristic peaks of GO at 1347 and 1585 cm^{-1} corresponding to the D-band and G-band of GO, respectively. Also, the I_D/I_G ratio of 0.833 for the as-synthesized GO showed the controlled rates of defects during synthesis, which is beneficial for further restoration of electrical conductivity of the GO through thermal annealing, as minimized defects could maintain the electrical conductivity of the reduced form of GO at optimum levels.[5, 6] The FESEM images of GO revealed the formation of 2D flakes with a large surface area (Figure S1 (d)). The HRTEM analysis also showed the successful exfoliation of GO and the formation of single-layer GO flakes (Figure S1 (e)) with a uniform basal plane with minor localized defects (Figure S1 (f)). The obtained results confirm the successful synthesis of GO flakes with desired features.

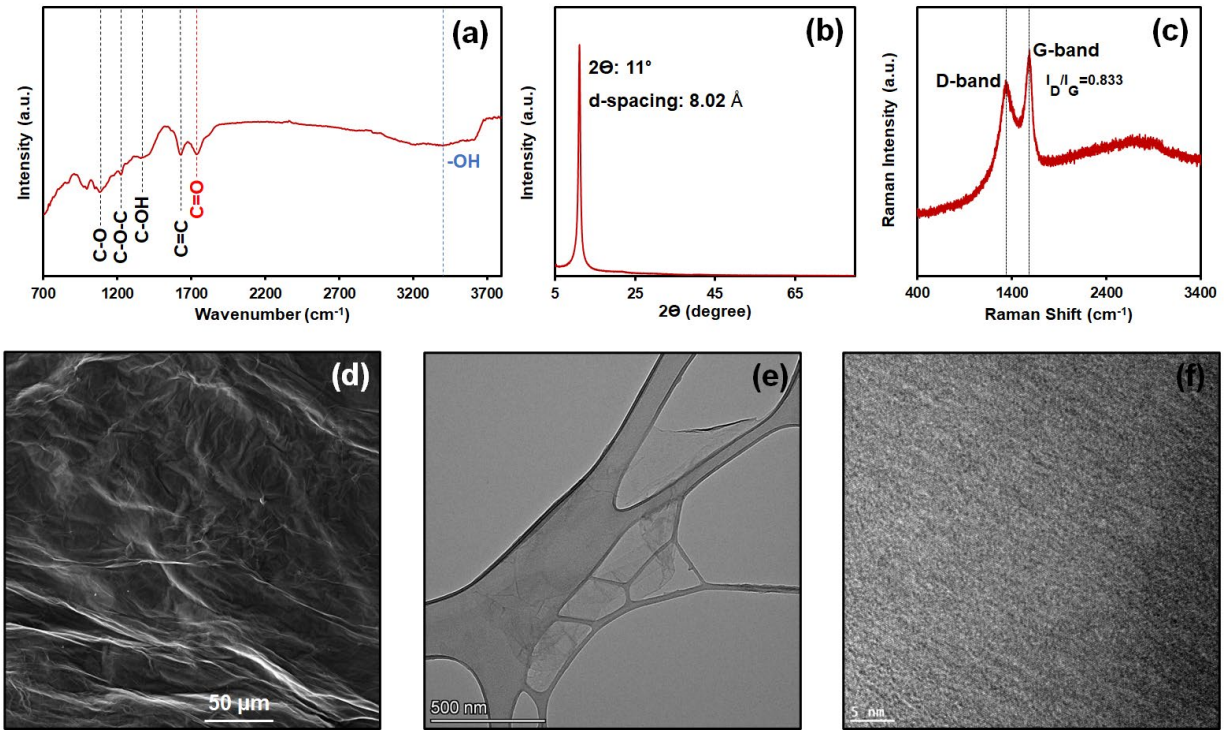

Figure S1. Characterization of the exfoliated GO flakes, including (a) FTIR, (b) X-ray diffractogram, (c) micro-Raman Spectroscopy, and (d) FESEM image. HRTEM images of well-exfoliated single-layer GO at (e) low magnification and (f) high magnification showing the atomic arrangement of the GO flakes.

The EDX analysis of the GO flakes showed an elemental composition of 51.2 wt% carbon, 45.9 wt % oxygen, and 2.5 wt% for the rest of the elements (sulfur and chlorine) with a homogeneous distribution of the elements through the GO flakes, as evidenced in the EDX mapping (Figure S2).

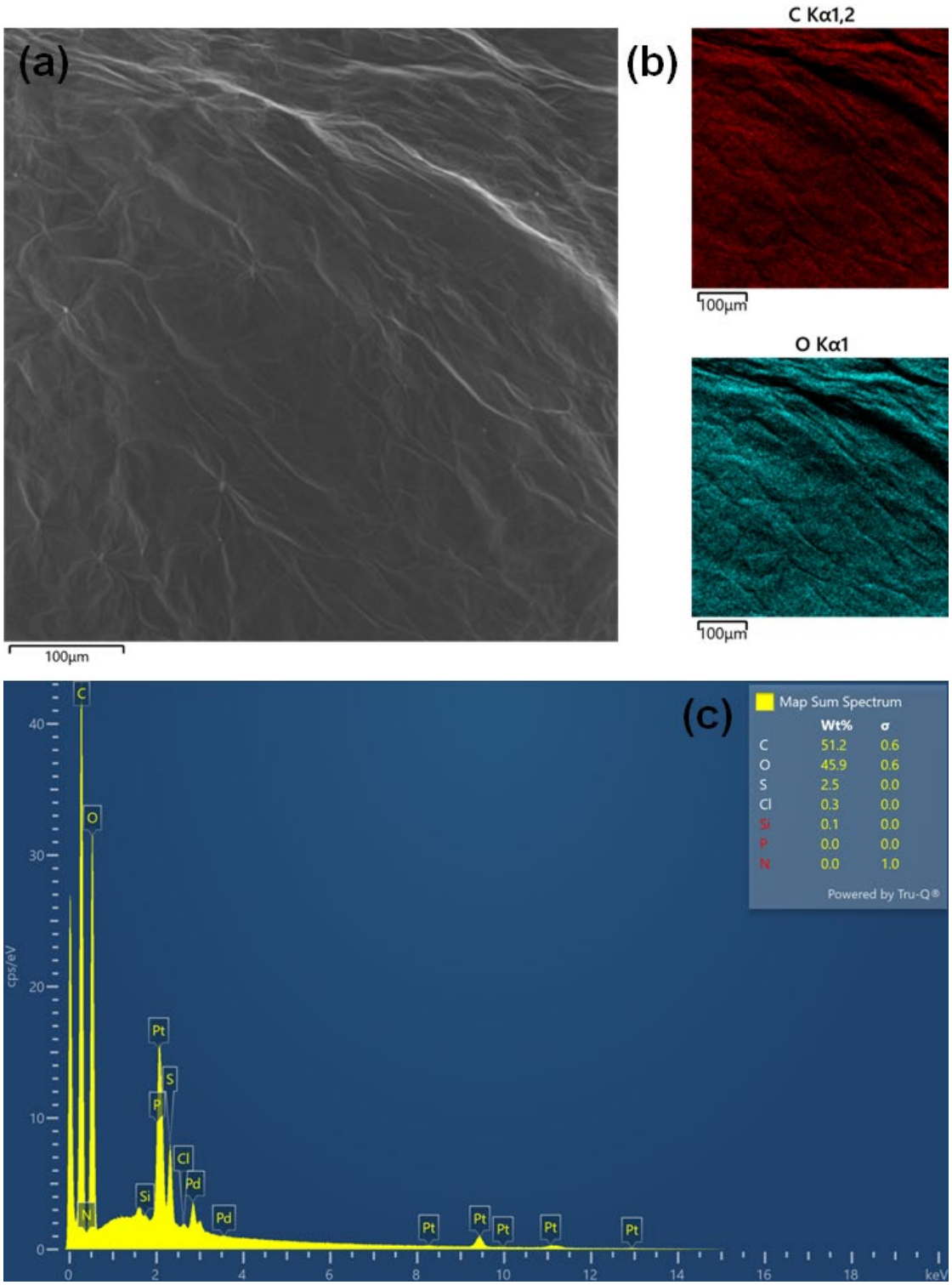

Figure S2. EDX analysis of GO, including (a) the scan area, (b) carbon and oxygen elemental distribution maps, and (c) the elemental distribution rate of GO.

4. From liquid templates to free-standing aerogels

Anti-reflection aerogels were generated through the interfacial complexation, allowing tunning of their structural features, spatial arrangement, and composition to yield on-demand liquid templates.[1] The 3D-structured filamentous aerogels' fabrication process starts from the liquid templating of low-concentration inks, i.e., GO (0.5-1 wt%, 5-10 mg mL^{-1}) and GO:CNF (weight ratio 1:1, 0.5-1 wt%), in the POSS-hexane domain. Upon pressure-adjusted extrusion of the inks into the POSS-hexane, a tubular liquid thread will be formed as a result of pH-dependent electrostatic interaction between the nanoparticles and ligands at the interface, preserving the liquid thread's shape in a non-equilibrium form by overcoming the applied pressure gradients and Plateau-Rayleigh instabilities. Accordingly, upon extrusion of the ink through the nozzle with an adjustable gauge number, the POSS molecules promptly assemble at the interface, generating a set of positively charged POSS-NH_3^+ assemblies, declining the interfacial tension and overcoming the instabilities. This allows the diffusion and subsequent assembly of GO at the interface through electrostatic interaction between its deprotonated carboxylic acid groups and ligand's (POSS) protonated amine groups.[7] This electrostatic interaction leads to the generation of hybrid nanoparticle surfactant assemblies and the jamming of nanoparticles, preserving the integrity of formed liquid templates through a solid-like skin around the liquid thread.[2] Freezing the formed liquid template at -85 °C for 24 h and the sublimation of the ice crystals through lyophilization forms free-standing filamentous aerogels. The extrusion of the aquatic inks in the POSS-hexane domain is demonstrated in Figures S3 (a) and (b), showing the formation of filamentous liquid template out of (c) GO and (d) GO:CNF inks. The structured liquid templates ((Figure S3 (c) and (d)) provide a scaffold for the fabrication of ultra-lightweight aerogels.

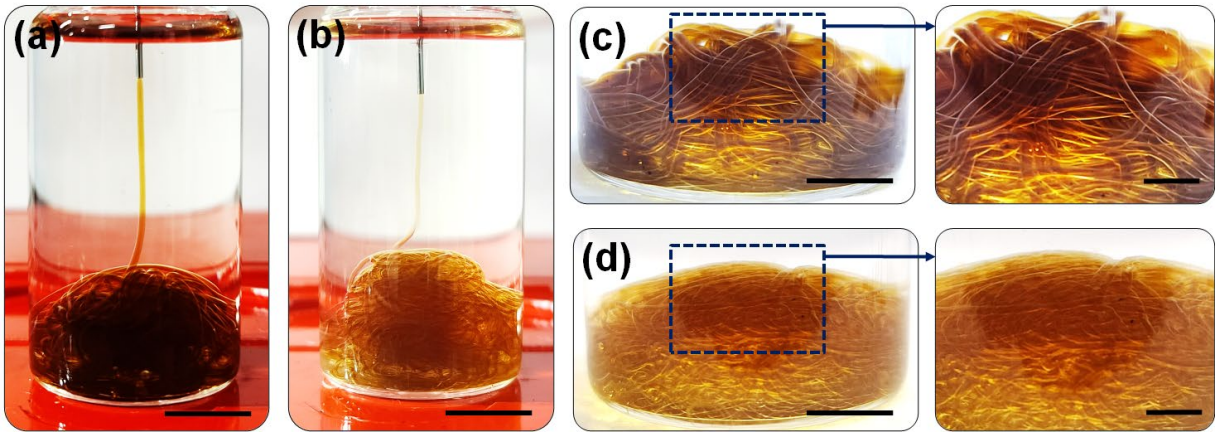

Figure S3. (a-d) Extrusion of the (a) GO (10 mg mL^{-1}) and (b) GO:CNF (1:1 weight ratio, 10 mg mL^{-1}) inks into the POSS-hexane medium. Formation of liquid constructs made of (c) GO and (d) GO:CNF inks as a template for aerogel production. Scale bars are equal to (a) ~ 11.31 mm, (b) ~ 11.62 mm, (c) ~ 7.13 mm, and zoom area ~ 2.79 mm, (d) ~ 7.35 mm, and zoom area ~ 3.70 mm. The demonstrated images in parts (a) to (d) were taken by a digital camera and their scale bars are approximate.

Minimization of the interfacial tension by the formed nanoparticle surfactant complexes at the liquid-liquid interface is the key to interfacial complexation and the formation of non-equilibrium-shaped filamentous liquid threads. The interfacial tension of the generated inks was measured via pendant drop tensiometry. Accordingly, the extrusion of the GO ink (1 mg mL^{-1}) into the hexane-containing POSS molecules declined the interfacial tension from around 49 mN/m for the neat hexane-water system [8, 9] to 1.90 mN/m (Figure S4). This implies the capability of the formed nanoparticle surfactant assemblies to minimize the interfacial tension toward preserving the filamentous shape of liquid templates and overcoming instabilities. This strengthening role of nanoparticle surfactants stems from the formation of a solid-like robust skin around the tubular liquid threads that could withstand the applied pressure gradients.

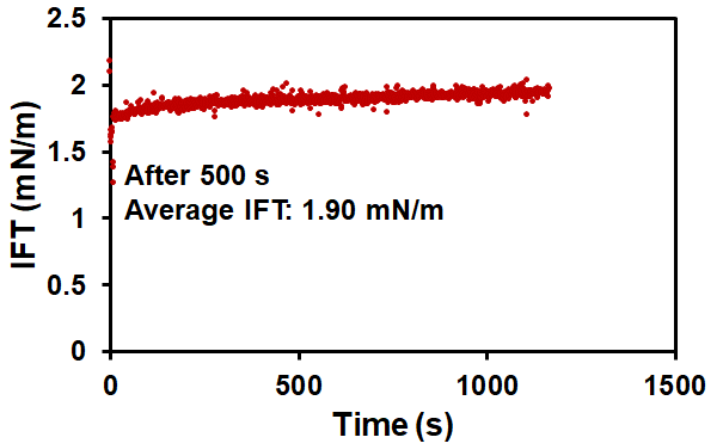

Figure S4. Dynamic interfacial tension of 1 mg mL^{-1} GO ink against the hexane-POSS medium.

The injection of the aqueous ink containing 1 mg mL^{-1} GO:CNF (1:1 weight ratio) into the pure non-polar hexane led to an interfacial tension of 38.97 mN/m. Whereas, the addition of POSS to the non-polar medium declined the interfacial tension to 4.48 mN/m, enabling liquid templating (Figure S5 (a) & (b)). These outcomes, along with the contraction of pendant drop of GO:CNF (1 mg mL^{-1}) ink in the hexane domain without POSS molecules, clearly revealed the inability of nanoparticles to jam at the interface (Figure S6 and Video S1). This implies the beneficial role of POSS molecules in interfacial complexation and fast diffusion toward the interface, causing the jamming of nanoparticles and generating a robust solid skin at the interface of two immiscible liquids.[8, 10]

The generated solid skin around the liquid thread was visualized via the contraction of the pendant drop upon injection of the aqueous GO (Figure S5 (c) and Video S2) or GO:CNF (Figure S5 (d) and Video S3) inks into the non-polar hexane domain containing 1 mg mL^{-1} POSS. As illustrated, decreasing the droplet volume leads to a decline in the interfacial areas, imposing compressive forces on the formed nanoparticle surfactant assemblies at the interface. This process was visualized as a result of wrinkles formation during the contraction of pendant droplets.

Notably, the observed wrinkles indicate the proper positioning of GO or GO:CNF by the POSS molecules at the interface that causes resilient thin interfacial films as a result of the overlapping of formed assemblies. This matter paves the way for fabricating green filamentous aerogels by embedding naturally harnessed fibrillated nanocellulose into the final structure.

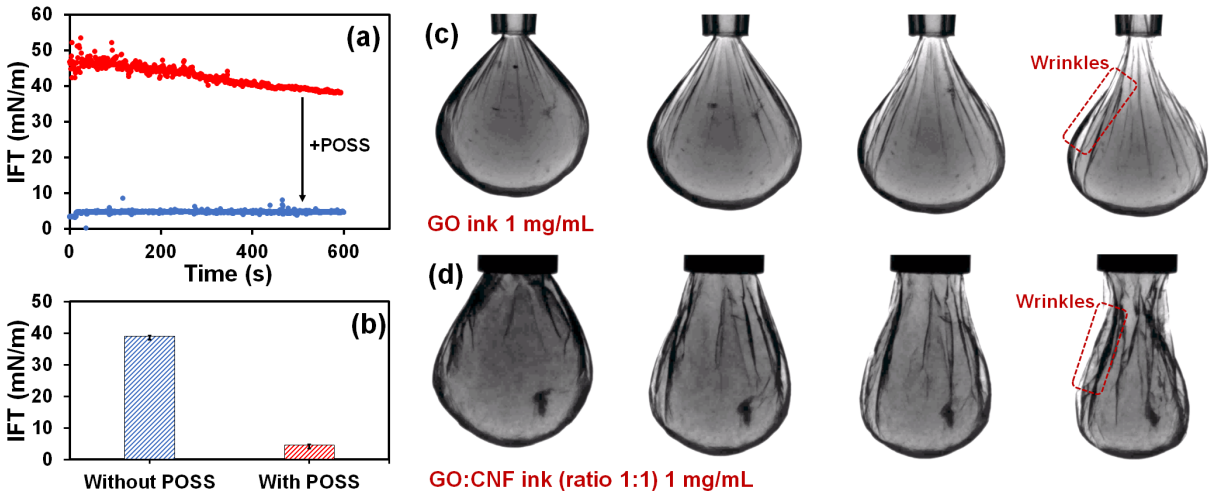

Figure S5. (a) Dynamic interfacial tension of the GO:CNF ink before and after the addition of POSS molecules as ligands. (b) The average interfacial tension of the GO:CNF ink against the hexane domain with and without POSS molecules. Contraction test of 1 mg mL^{-1} (c) GO and (d) GO:CNF ink in the extrusion medium (1 mg mL^{-1} POSS in hexane); the formation of the wrinkles around the droplets indicates the generation of robust assemblies at the interface capable of withstanding the applied forces and overcome the instabilities. This enables the liquid threads to preserve their integrity in a non-equilibrium filamentous form.

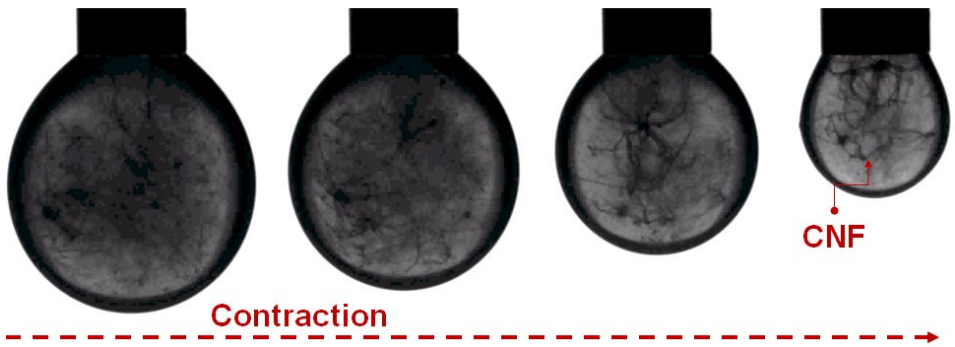

Figure S6. Contraction of pendant drop related to 1 mg mL^{-1} GO:CNF ink (1:1 ratio) against pure hexane without POSS.

Moreover, varying the injection needle's gauge number from 15 to 27 significantly declined the average diameter of the filaments after lyophilization, which can be a great asset for applications such as EM shielding by improving the number of interfaces per volume of the aerogel (Figure S7). This change in the gauge number of needles could be used as a governing factor to tune the distance between the filaments and the number of filaments per volume, significantly increasing the number of interfaces toward a more robust EM wave attenuation.

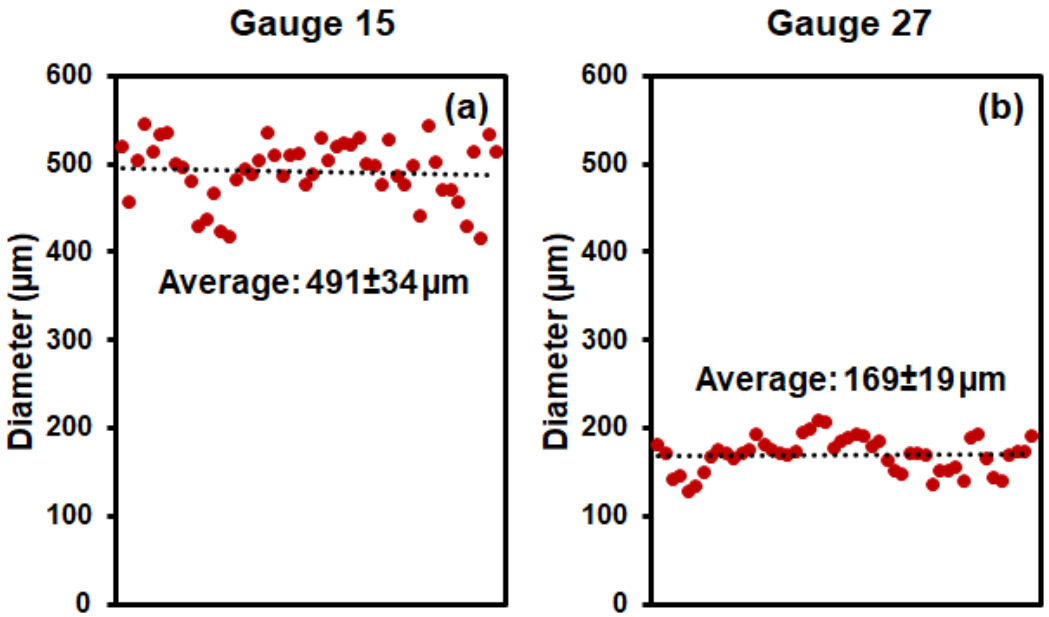

Figure S7. The average diameter of GO-CNF aerogels prepared via an injection needle with a gauge number of (a) 15 and (b) 27.

Likewise, an increase in the concentration of the ink during liquid templating can alter the micro-scale porosities within the core of the filaments. As demonstrated in Figure S8, an increase in the concentration of GO:CNF ink (1:1 weight ratio) from 5 mg mL^{-1} to 10 mg mL^{-1}, considerably increases the number of micro-scale porosities per volume of the filament and reduces the average pore size from about 58.01±17.55 to 41.13±15.47. Such tunability of the aerogel construct allows engineering the porosities at multi-scale, and as a result, governing the shielding mechanism of

the final construct. Of note, for micro-scale porosity assessment, the GO-CNF aerogels were made through molding, freezing, and lyophilization of different concentrations of GO:CNF inks.

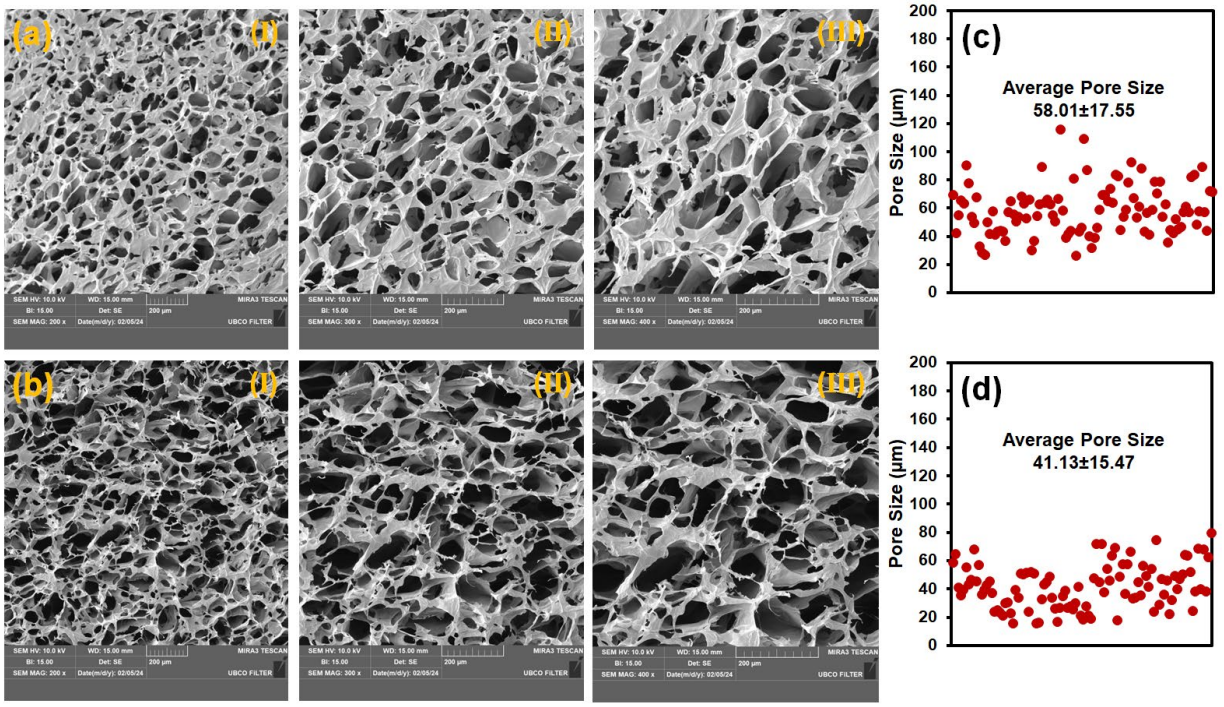

Figure S8. Pore size distribution assessment of the samples via FESEM analysis; the FESEM images of GO-CNF aerogels composed of (a) 5 mg mL^{-1} and (b) 10 mg mL^{-1} GO:CNF (1:1 weight ratio) at different zooms (I) 200x, (II) 300x, and (III) 400x. The pore size distribution and average pore size of the GO-CNF aerogel consisted of (c) 5 mg mL^{-1} and (d) 10 mg mL^{-1} GO:CNF (1:1 weight ratio), each obtained from the assessment of various spots of three different samples. The FESEM images showcase an obvious rise in the concentration of porosities per volume of the aerogel and a notable decline in the average pore size and pore size distribution upon an increase in the concentration of GO:CNF ink.

4.1. Aerogels characterization

Proof of GO and CNF integration in the formed hierarchical porous framework was provided through supporting X-ray diffraction (XRD) and micro-Raman spectroscopy, before and after reduction. The assessment outcomes confirmed the assembly of nanoparticles in the hierarchical arrangement and restoration of the conductive carbonaceous pathway. The XRD analysis was

performed via parallel beam technique, using a polycapillary collimating optic to assess the hierarchal structure of the aerogel framework. As shown in Figure S9, the X-ray diffractogram of GO aerogel showed a well-defined sharp 2Θ peak at 10.7°, corresponding to the interlayer spacing (d-spacing) of 8.2 Å attributed to the (001) crystalline plane of GO. This increase in the d-spacing compared with neat graphite (3.4 Å) arises from formed oxygen-based functional groups on the GO.[11] The other broad peak at 2Θ of 25.2°, attributed to the d-spacing of 3.5 Å, appeared as a result of GO flakes stacking in the aerogel framework.[12] Upon thermal annealing of the GO aerogel at 800 °C under Ar for 1 h, the peak of rGO aerogel shifted to 2Θ of 25.9° corresponding to the d-spacing of 3.4 Å. This interlayer spacing matches the d-spacing of graphite, showcasing the removal of the oxygen-based functional groups and restoration of the carbonaceous structure through graphitization. Such treatment restores the conjugation of the sp^2 regions and leads to well-oriented stacking arrangements among the graphene flakes.[11, 13] The X-ray diffractogram of GO-CNF aerogel also demonstrated a hybrid aerogel framework composed of GO and fibrillated nanocellulose by showcasing the main fingerprint peaks of GO and CNF. Correspondingly, the sharp peak at 2Θ of 10.6° originated from the assembled GO flakes in the framework, attributed to the d-spacing of 8.3 Å. Whereas the (002) crystalline plane of native cellulose (JCPDS 03-0289) appeared at 2Θ of 22.3, corresponding to the interlayer spacing of 3.9 Å. The reduction of GO-CNF (rGO-CNF) aerogel at 800 °C under Ar completely changed its X-ray diffractogram, showcasing a broad peak at 2Θ of 25.7° attributed to the d-spacing of 3.4 Å. This outcome vividly illuminates the removal of the oxygen-based functional groups and the formation of a 3D stacked arrangement between the fibrillated nanocellulose and graphene flakes.

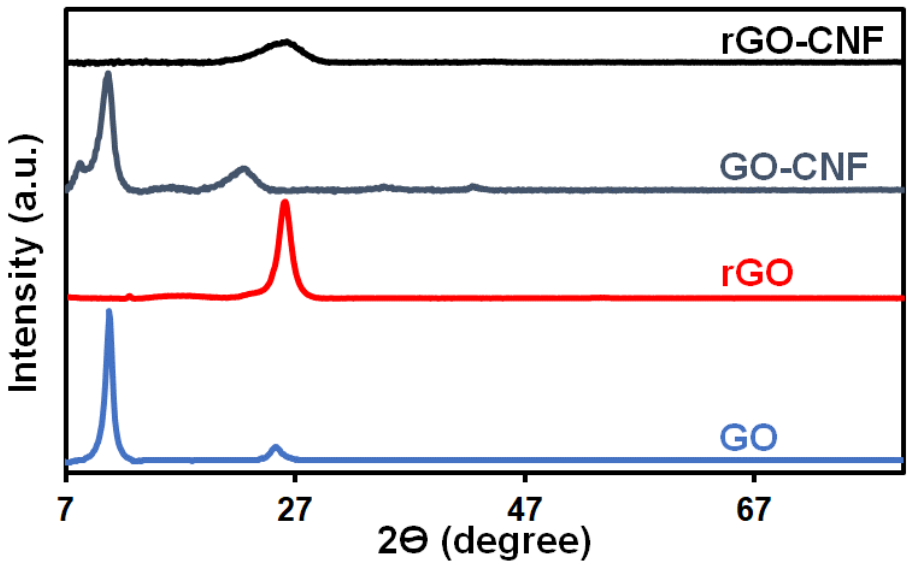

Figure S9. X-ray diffractograms of aerogels before and after thermal annealing. Reprinted with permission from reference [1] under Creative Commons CC BY-NC 3.0 license. Of note, the baseline of the X-ray diffractograms was removed via further post-processing.

The micro-Raman spectroscopy showcased two well-defined peaks for all reduced and non-reduced aerogels between regions 1334-1348 cm^{-1} and 1585-1598 cm^{-1}, corresponding to the D-band and G-band of either GO or thermally annealed GO, assembled within the 3D hierarchical framework (Figure S10). As demonstrated, the GO aerogel showed I_D/I_G of 0.98, which elevated to 1.03 after thermal annealing, indicating a slight rise in the structural defects as a result of functional group detachment. However, the GO-CNF aerogels showcased lower defect rates than the GO or rGO aerogels, revealing an I_D/I_G ratio of 0.85 and 0.93 before and after thermal annealing. The above outcomes support the outcomes of X-ray diffractograms and confirm the existence of either GO or rGO in the hierarchical framework of aerogels.

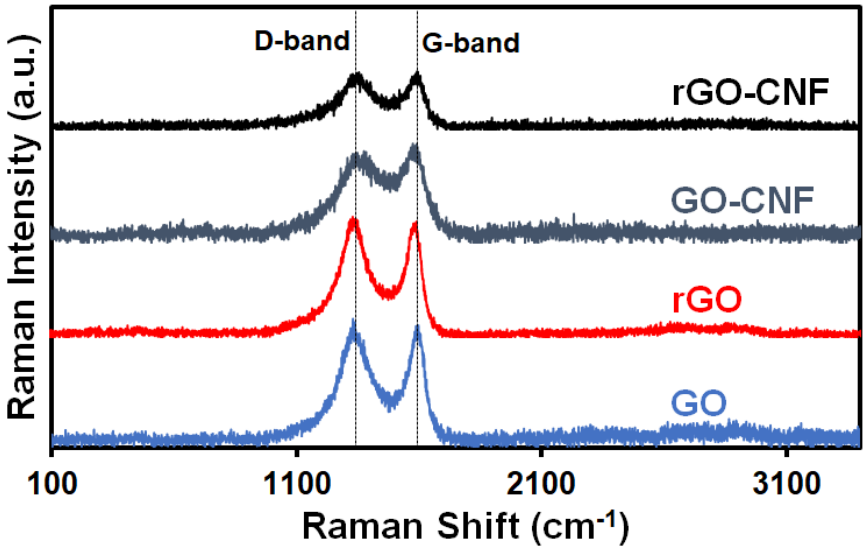

Figure S10. Micro-Raman spectroscopy results of aerogels before and after thermal annealing.

5. Electromagnetic shielding data

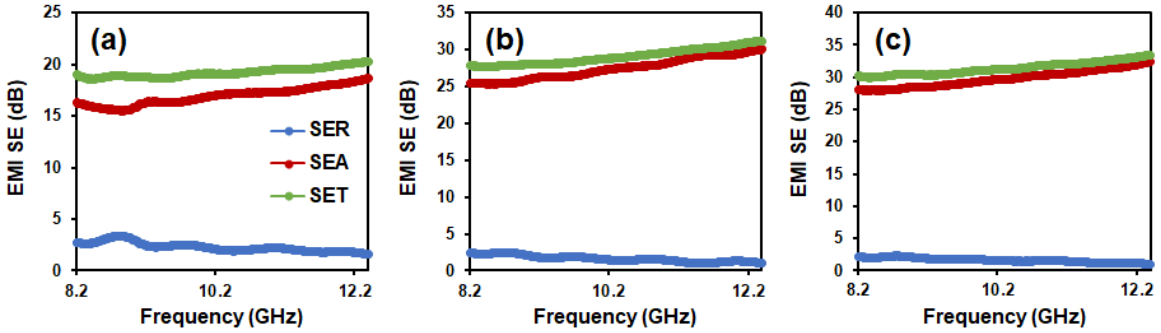

Figure S11. EMI SE characteristic of rGO-CNF aerogel prepared with 0.5 wt% ink at (a) 2 mm, (b) 4 mm, and (c) 6 mm thicknesses.

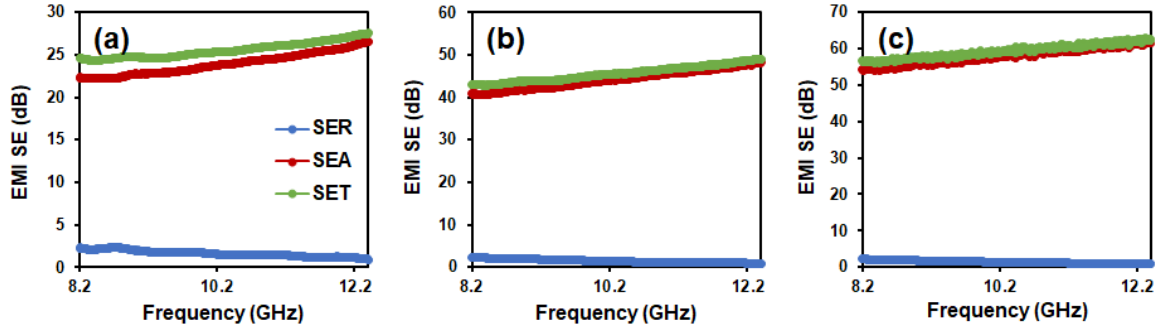

Figure S12. EMI SE characteristic of rGO-CNF aerogel prepared with 1 wt% ink at (a) 2 mm, (b) 4 mm, and (c) 6 mm thicknesses.

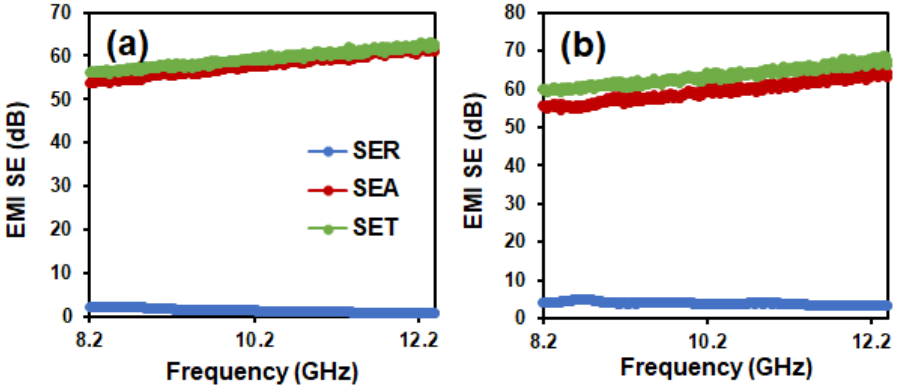

Figure S13. EMI SE characteristic of 6 mm thick rGO-CNF aerogel prepared with 1 wt% ink with (a) small and (b) large filaments.

Table S1. EMI shielding performance of the rGO-CNF aerogel with large and small filaments compared to recently developed porous constructs.

Sample	Thickness (mm)	EMI SE (dB)	SE_R (dB)	R	A	Ref.
Hybrid core-shell CNT-graphene foam	1.6	38.4	3.9	0.59	0.41	[14]
MWCNTs-WPU foam	2.3	50.5	~9	~0.89	~0.11	[15]
CNT sponge-epoxy	2	44	5	~0.68	~0.32	[16]
Hybrid AgNWs-carbon sponge	3	70.1	~11	~0.91	~0.09	[17]
CNTs-rGO foam	2	31.2	5.9	0.74	0.26	[18]
rGO foam	0.9	42.3	10	0.9	0.1	[19]
Ti_2CT_x-PVA foam	5	28	2	0.37	0.63	[20]
$Ti_3C_2T_x$-PEDOT:PSS aerogels	5	28	3	0.5	0.5	[21]
Honeycomb-structured porous graphene-AgNWs	0.0483	61.8	~14.5	~0.96	~0.04	[22]
AgNWs-nanocellulose aerogels	2	70.5	~17	~0.98	~0.02	[23]
Hybrid CNTs-ANFs aerogel	0.568	54.4	~8	~0.84	~0.16	[24]
Core-shell Cu NWs-graphene aerogel	5	43.7	2.86	~0.48	~0.52	[25]
Core-shell compressed Cu NWs-graphene aerogel	5	31.28	4.11	~0.61	~0.39	[25]
$Ti_3C_2T_x$-rGO aerogel	2	56.4	5.7	0.73	0.27	[26]
Carbonized wood-Ni-CNTs	-	48.2	2.8	~0.47	~0.53	[27]
Graphene-boron nitride nanoribbons aerogel	2	70	~12	~0.8	~0.2	[28]
rGO-CNF aerogel	2	25.54	1.62	0.30	0.68	
rGO-CNF aerogel	4	45.62	1.43	0.27	0.72	**This Work**
rGO-CNF aerogel	6	59.32	1.38	0.26	0.73	

Abbreviations: Carbon nanotube (CNT), multi-walled carbon nanotube (MWCNT), water-borne polyurethane (WPU), silver nanowires (AgNWs), reduced graphene oxide (rGO), polyvinyl alcohol (PVA), poly(3,4-ethylenedioxythiophene) polystyrene sulfonate (PEDOT:PSS), nanowires (NWs).

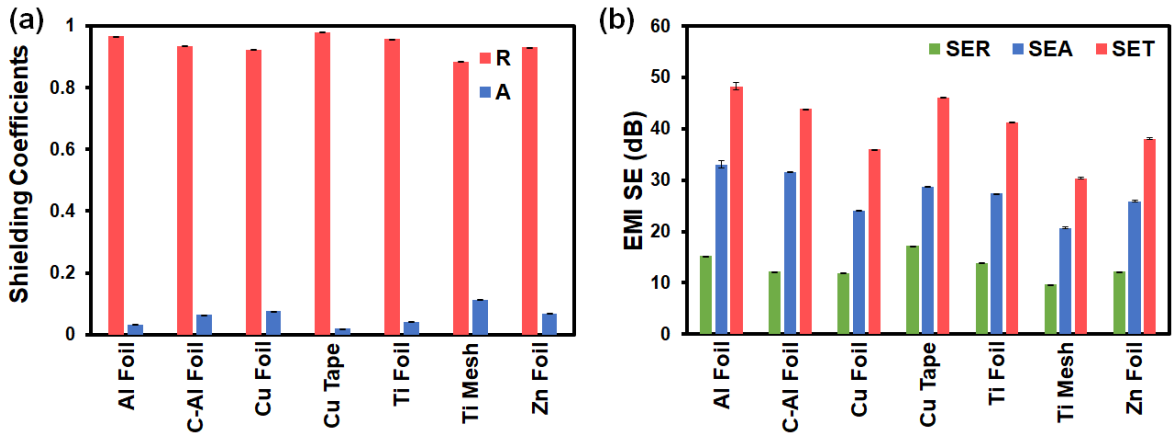

Figure S14. (a) Shielding coefficients (reflectance (R) and absorbance (A)) and (b) shielding parameters (reflection loss (SE_R), absorption loss (SE_A), and total specific shielding (SE_T)) of used metallic foils, mesh, or tape.

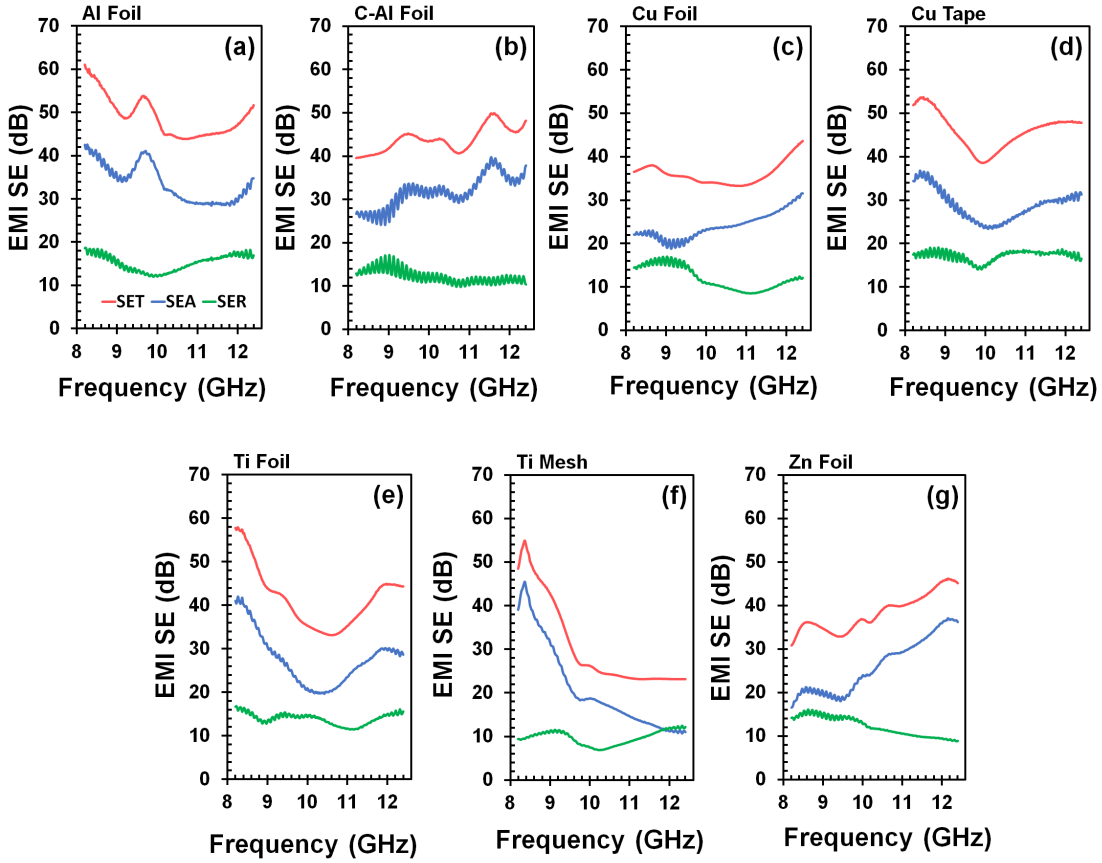

Figure S15. EMI SE of (a) Al foil (thickness (t):15 µm), (b) carbon-coated Al (C-Al) foil (t:15 µm), (c) Cu foil (t:10 µm), (d) Cu tape (t:50 µm), (e) Ti foil (t:20 µm), (f) Ti mesh (t:426 µm), and (g) Zn foil (t:106 µm) over the X-band frequency range (8.2-12.4 GHz).

Table S2. Shielding parameters and coefficients of metallic substrates; the recorded parameters are average of four assessments in the whole X-band frequency range (8.2-12.4 GHz).

Metallic Substrate	Thickness (μm)	Shielding Coefficients		EMI SE (dB)		
		A	R	SE_R	SE_A	SE_T
Al foil	15	0.03	0.96	15.23	33.02	48.25
C-Al foil	15	0.06	0.93	12.21	31.64	43.85
Cu foil	10	0.07	0.92	11.95	24.02	35.98
Cu tape	50	0.01	0.98	17.23	28.76	46.00
Ti foil	20	0.04	0.95	13.92	27.40	41.33
Ti mesh	426	0.11	0.88	9.67	20.71	30.39
Zn foil	106	0.06	0.93	12.15	25.92	38.08

Table S3. Shielding parameters and coefficients of hybrid aerogel (6 mm thick rGO-CNF (1 wt%))-metallic substrates shielding system; the recorded parameters are average of four assessments in the whole X-band frequency range (8.2-12.4 GHz).

Metallic Substrate	Shielding Coefficients		EMI SE (dB)		
	A	R	SE_R	SE_A	SE_T
rGO-CNF Aerogel	0.71	0.28	1.46	51.61	53.07
rGO-CNF Aerogel/Al foil	0.75	0.24	1.20	88.11	89.32
rGO-CNF Aerogel/C-Al foil	0.79	0.20	0.99	84.53	85.52
rGO-CNF Aerogel/Cu foil	0.71	0.28	1.46	85.46	86.93
rGO-CNF Aerogel/Cu tape	0.73	0.26	1.36	83.39	84.76
rGO-CNF Aerogel/Ti foil	0.70	0.29	1.54	82.55	84.09
rGO-CNF Aerogel/Ti mesh	0.81	0.18	0.87	57.98	58.85
rGO-CNF Aerogel/Zn foil	0.76	0.23	1.15	72.83	73.98

Table S4. The developed hybrid aerogel-metallic substrate shields compared with the recently developed shielding systems.

Shield Composition	Thickness (mm)	A	SE_R (dB)	EMI SE (dB)	Ref.
$Ti_3C_2T_x$	0.014	~0.01	~20	82	[29]
$Ti_3C_2T_x$	0.005	~0.02	17.5	57.4	[30]
Ti_3CNT_x	0.005	~0.02	17	49.7	[30]
$Ti_3C_2T_x$	0.001	~0.04	13.5	46.1	[31]
$Ti_3C_2T_x$	0.02	<0.01	27	68	[32]
$Ti_3C_2T_x$/gelation	0.004	~0.02	~19.2	53.6	[33]
ANF-$Ti_3C_2T_x$	0.018	0.1	10.3	55.9	[34]
ANF-$Ti_3C_2T_x$	0.037	~0.02	~18	48	[35]
CNF-$Ti_3C_2T_x$	0.074	~0.29	5.3	25.8	[36]
BC-$Ti_3C_2T_x$	0.006	0.01	17	37.3	[37]
Multilayer CNF-$Ti_3C_2T_x$	0.035	0.02	17.7	39.6	[38]
PVA foam-$Ti_3C_2T_x$	5	0.63	2	28	[20]
PVA-$Ti_3C_2T_x$	0.3	0.09	11	21	[20]
Multilayer PVA-$Ti_3C_2T_x$	0.027	0.15	8.3	44.4	[39]
PS-$Ti_3C_2T_x$	2	~0.22	6.5	61.2	[40]
PCC-$Ti_3C_2T_x$-PVA	-	0.01	19.13	70.08	[41]
Polyolefin- $Ti_3C_2T_x$-Graphene	1.85 mm	0.11	9.23	60.98	[42]
Polyimide-$Ti_3C_2T_x$ Hollow microspheres	-	0.005	23	85	[43]
Latex-SWCNT-$Ti_3C_2T_x$	1.1	~0.02	~19	52	[44]
PVDF-PANi-$Ti_3C_2T_x$	1.7	0.3	5.2	33.3	[45]
PEDOT:PSS-$Ti_3C_2T_x$ aerogel	5	0.5	3	28	[21]

PEDOT:PSS-$Ti_3C_2T_x$ hydrogel	0.295	0.42	3.7	51.7	[46]
rGO-$Ti_3C_2T_x$ aerogel	2	0.27	5.7	56.4	[26]
CF-$Ti_3C_2T_x$	0.343	~0.03	~15	45.7	[47]
PANi-CF-$Ti_3C_2T_x$	0.55	0.26	5.7	26.5	[48]
PD-$Ti_3C_2T_x$	0.007	~0.03	~16	58.4	[49]
XG-$Ti_3C_2T_x$	0.012	~0.03	~15	40.1	[50]
rGO film	0.0084	~0.16	~8	20	[51]
Graphene fiber	0.0263	0.11	~9	56	[52]
rGO-liquid metal	0.033	0.006	22	80	[53]
rGO-CNT foam	2	0.26	5.9	31.2	[18]
PDMS-rGO	5	0.51	2.99	26	[8]
rGO foam	0.9	0.1	10	42.3	[19]
Graphene-Fe_3O_4	0.25	0.16	8	24	[54]
Graphene-CuNWs aerogel	5	~0.52	2.86	43.7	[25]
Compressed Graphene CuNWs aerogel	5	~0.39	4.11	31.28	[25]
Graphite film	~0.0004	~0.31	~5	27.8	[55]
Anisotropically oriented carbon films	480 nm	0.16	7.96	21.72	[56]
PMMA-graphene-MWCNT	2	0.22	6.67	36	[57]
Multilayer WPU-rGO-Fe_3O_4-MWCNT	0.8	0.73	1.46	36	[58]
PMMA-rGO-Fe_3O_4	2.9	0.4	4	29.3	[59]
rGO-AgNWs network	~0.0001	~0.16	8.1	35	[60]
rGO-$(C\text{-}SiC)_n$ (n=1, 3, and 12)	4	~0.06	~12	70.2	[61]
Graphene-CNT core-shell foam	1.6	0.41	3.9	38.4	[14]
WPU-MWCNTs foam	2.3	~0.11	~9	50.5	[15]
Epoxy-CNT sponge	2	~0.32	5	44	[16]
Epoxy-MWCNT-Fe_3O_4-Ag	2	0.35	4.5	35	[62]
PLLA-MWCNT	1.5	0.4	4	30	[63]
PVDF-MWCNT	1	0.23	6.3	22.5	[64]
WPU-MWCNT	2.3	~0.2	~7.2	46.7	[65]
ANF-CNT hybrid aerogel	0.568	~0.16	~8	54.4	[24]
ANF-CNT	0.024	~0.04	~14	36	[66]
GTR-CNT	1	0.25	6	30	[67]
ANF-PVA hydrogel-AgNWs-PVA	~0.3	~0.03	16	52	[68]
CNF-AgNWs aerogel	4	~0.03	15	70	[23]
Leather-AgNWs	0.5	~0.16	~8	55	[69]
Carbon-AgNWs sponge	3	~0.09	~11	70.1	[17]
Porous honeycomb graphene-AgNWs	0.0483	~0.04	~14.5	61.8	[22]
AgNWs aerogel	3	~0.01	20	109.3	[70]
Cu nanosheets	0.063	~0.04	~14	105	[71]
Porous 2D Cu nanosheets	0.015	0.1	10	100	[71]
Electroless plating Cu NPs-PU nanofiber	0.015	0.001	29.55	63.5	[72]
rGO-CNF Aerogel	6	0.71	1.46	53.07	
rGO-CNF Aerogel/Al foil	6+0.015	0.75	1.20	89.32	
rGO-CNF Aerogel/C-Al foil	6+0.015	0.79	0.99	85.52	
rGO-CNF Aerogel/Cu foil	6+0.010	0.71	1.46	86.93	**This Study**
rGO-CNF Aerogel/Cu tape	6+0.050	0.73	1.36	84.76	
rGO-CNF Aerogel/Ti foil	6+0.020	0.70	1.54	84.09	
rGO-CNF Aerogel/Ti mesh	6+0.426	0.81	0.87	58.85	
rGO-CNF Aerogel/Zn foil	6+0.106	0.76	1.15	73.98	

Abbreviations: Aramid nanofibers (ANF), cellulose nanofiber (CNF), bacterial cellulose (BC), polyvinyl alcohol (PVA), polystyrene (PS), phase change capsules (PCC), single-walled carbon nanotubes (SWCNT), poly(vinylidene fluoride) (PVDF), poly(3,4-ethylenedioxythiophene) polystyrene sulfonate (PEDOT:PSS), reduced graphene oxide (rGO), carbon fiber (CF), polyaniline (PANi), polydopamine (PD), xanthan gum (XG), carbon nanotube (CNT), polydimethylsiloxane (PDM), copper nanowires (CuNWs), poly (methyl methacrylate) (PMMA), multi-walled carbon

nanotube (MWCNT), water-borne polyurethane (WPU), silver nanowires (AgNWs), poly(L-lactide) (PLLA), ground tire rubber (GTR), nanoparticles (NPs), and polyurethane (PU).

References

1. S. A. Hashemi, A. Ghaffarkhah, M. Goodarzi, A. Nazemi, G. Banvillet, A. S. Milani, M. Soroush, O. J. Rojas, S. Ramakrishna, S. Wuttke, T. P. Russell, M. Kamkar and M. Arjmand, *Advanced Materials*, 2023, 2302826.
2. A. Ghaffarkhah, S. A. Hashemi, S. Rostami, M. Amini, F. Ahmadijokani, A. Pournaghshband Isfahani, S. E. Mhatre, O. J. Rojas, M. Kamkar, S. Wuttke, M. Soroush and M. Arjmand, *Advanced Functional Materials*, 2023, 2304748.
3. S. A. Hashemi, S. Bahrani, S. M. Mousavi, N. Omidifar, N. G. G. Behbahan, M. Arjmand, S. Ramakrishna, A. M. Dimiev, K. B. Lankarani and M. Moghadami, *Talanta*, 2022, **239**, 123113.
4. S. A. Hashemi, H. R. Naderi, S. M. Mousavi, S. Bahrani, M. Arjmand, A. M. Dimiev and S. Ramakrishna, *Carbon*, 2022, **188**, 276-288.
5. M. Pimenta, G. Dresselhaus, M. S. Dresselhaus, L. Cancado, A. Jorio and R. Saito, *Physical Chemistry Chemical Physics*, 2007, **9**, 1276-1290.
6. K. K. H. De Silva, P. Viswanath, V. K. Rao, S. Suzuki and M. Yoshimura, *The Journal of Physical Chemistry C*, 2021, **125**, 7791-7798.
7. S. Shi and T. P. Russell, *Advanced Materials*, 2018, **30**, 1800714.
8. M. Kamkar, A. Ghaffarkhah, R. Ajdary, Y. Lu, F. Ahmadijokani, S. E. Mhatre, E. Erfanian, U. Sundararaj, M. Arjmand and O. J. Rojas, *Small*, 2022, 2200220.
9. F. Kim, L. J. Cote and J. Huang, *Adv. Mater.*, 2010, **22**, 1954-1958.
10. S. Shi, B. Qian, X. Wu, H. Sun, H. Wang, H. B. Zhang, Z. Z. Yu and T. P. Russell, *Angewandte Chemie International Edition*, 2019, **58**, 18171-18176.
11. C. B. Li, Y. J. Li, Q. Zhao, Y. Luo, G. Y. Yang, Y. Hu and J. J. Jiang, *ACS Applied Materials & Interfaces*, 2020, **12**, 30686-30694.
12. W. L. Song, X. T. Guan, L. Z. Fan, W. Q. Cao, C. Y. Wang and M. S. Cao, *Carbon*, 2015, **93**, 151-160.
13. Q. Zhang, X. Xu, H. Li, G. Xiong, H. Hu and T. S. Fisher, *Carbon*, 2015, **93**, 659-670.
14. Q. Song, F. Ye, X. Yin, W. Li, H. Li, Y. Liu, K. Li, K. Xie, X. Li and Q. Fu, *Adv. Mater.*, 2017, **29**, 1701583.
15. Z. Zeng, H. Jin, M. Chen, W. Li, L. Zhou and Z. Zhang, *Adv. Funct. Mater.*, 2016, **26**, 303-310.
16. Y. Chen, H. B. Zhang, Y. Yang, M. Wang, A. Cao and Z. Z. Yu, *Adv. Funct. Mater.*, 2016, **26**, 447-455.
17. Y. J. Wan, P. L. Zhu, S. H. Yu, R. Sun, C. P. Wong and W. H. Liao, *Small*, 2018, **14**, 1800534.

18. L. Kong, X. Yin, H. Xu, X. Yuan, T. Wang, Z. Xu, J. Huang, R. Yang and H. Fan, *Carbon*, 2019, **145**, 61-66.

19. B. Shen, Y. Li, D. Yi, W. Zhai, X. Wei and W. Zheng, *Carbon*, 2016, **102**, 154-160.

20. H. Xu, X. Yin, X. Li, M. Li, S. Liang, L. Zhang and L. Cheng, *ACS Appl. Mater. Interfaces.*, 2019, **11**, 10198-10207.

21. G. Y. Yang, S. Z. Wang, H. T. Sun, X. M. Yao, C. B. Li, Y. J. Li and J. J. Jiang, *ACS Applied Materials & Interfaces*, 2021, **13**, 57521-57531.

22. J. Xu, R. Li, S. Ji, B. Zhao, T. Cui, X. Tan, G. Gou, J. Jian, H. Xu and Y. Qiao, *ACS Nano*, 2021, **15**, 8907-8918.

23. Z. Zeng, T. Wu, D. Han, Q. Ren, G. Siqueira and G. Nyström, *ACS Nano*, 2020, **14**, 2927-2938.

24. P. Hu, J. Lyu, C. Fu, W.-b. Gong, J. Liao, W. Lu, Y. Chen and X. Zhang, *ACS Nano*, 2019, **14**, 688-697.

25. S. Wu, M. Zou, Z. Li, D. Chen, H. Zhang, Y. Yuan, Y. Pei and A. Cao, *Small*, 2018, **14**, 1800634.

26. S. Zhao, H. B. Zhang, J. Q. Luo, Q. W. Wang, B. Xu, S. Hong and Z. Z. Yu, *ACS Nano*, 2018, **12**, 11193-11202.

27. B. Zhao, P. Bai, M. Yuan, Z. Yan, B. Fan, R. Zhang and R. Che, *Carbon*, 2022.

28. L. Feng, P. Wei, Q. Song, J. Zhang, Q. Fu, X. Jia, J. Yang, D. Shao, Y. Li and S. Wang, *ACS Nano*, 2022, **16**, 17049-17061.

29. H. Chen, Y. Wen, Y. Qi, Q. Zhao, L. Qu and C. Li, *Adv. Funct. Mater.*, 2020, **30**, 1906996.

30. M. Han, C. E. Shuck, R. Rakhmanov, D. Parchment, B. Anasori, C. M. Koo, G. Friedman and Y. Gogotsi, *ACS Nano*, 2020, **14**, 5008-5016.

31. J. Zhang, N. Kong, S. Uzun, A. Levitt, S. Seyedin, P. A. Lynch, S. Qin, M. Han, W. Yang and J. Liu, *Adv. Mater.*, 2020, 2001093.

32. M. Ying, R. Zhao, X. Hu, Z. Zhang, W. Liu, J. Yu, X. Liu, X. Liu, H. Rong and C. Wu, *Angewandte Chemie*, 2022, **134**, e202201323.

33. X. Huang, J. Huang, G. Zhou, Y. Wei, P. Wu, A. Dong and D. Yang, *Small*, 2022, 2200829.

34. J. Lu, L. Cheng, C. Liao, P. Jia, L. Song, B. Wang and Y. Hu, *Adv. Mater. Interfaces.*, 2022, 2101359.

35. J. Wang, X. Ma, J. Zhou, F. Du and C. Teng, *ACS Nano*, 2022, **16**, 6700-6711.

36. W. T. Cao, F. F. Chen, Y. J. Zhu, Y. G. Zhang, Y. Y. Jiang, M. G. Ma and F. Chen, *ACS Nano*, 2018, **12**, 4583-4593.

37. Y. Wan, P. Xiong, J. Liu, F. Feng, X. Xun, F. M. Gama, Q. Zhang, F. Yao, Z. Yang and H. Luo, *ACS Nano*, 2021, **15**, 8439-8449.

38. B. Zhou, Z. Zhang, Y. Li, G. Han, Y. Feng, B. Wang, D. Zhang, J. Ma and C. Liu, *ACS Appl. Mater. Interfaces.*, 2020, **12**, 4895-4905.

39. X. Jin, J. Wang, L. Dai, X. Liu, L. Li, Y. Yang, Y. Cao, W. Wang, H. Wu and S. Guo, *Chem. Eng. J.*, 2020, **380**, 122475.

40. R. Sun, H. B. Zhang, J. Liu, X. Xie, R. Yang, Y. Li, S. Hong and Z. Z. Yu, *Adv. Funct. Mater.*, 2017, **27**, 1702807.

41. S. Gong, X. Sheng, X. Li, M. Sheng, H. Wu, X. Lu and J. Qu, *Advanced Functional Materials*, 2022, **32**, 2200570.

42. X. Tan, T. H. Liu, W. Zhou, Q. Yuan, J. Ying, Q. Yan, L. Lv, L. Chen, X. Wang and S. Du, *ACS Nano*, 2022, **16**, 9254-9266.

43. Y. Zhang, K. Ruan, K. Zhou and J. Gu, *Advanced Materials*, 2023, **35**, 2211642.

44. Y. Li, X. Tian, S. P. Gao, L. Jing, K. Li, H. Yang, F. Fu, J. Y. Lee, Y. X. Guo and J. S. Ho, *Adv. Funct. Mater.*, 2020, **30**, 1907451.

45. S. Habibpour, K. Zarshenas, M. Zhang, M. Hamidinejad, L. Ma, C. B. Park and A. Yu, *ACS Appl. Mater. Interfaces.*, 2022.

46. J. Liu, L. Mckeon, J. Garcia, S. Pinilla, S. Barwich, M. Möbius, P. Stamenov, J. N. Coleman and V. Nicolosi, *Advanced Materials*, 2022, **34**, 2106253.

47. K. Wang, C. Chen, Q. Zheng, J. Xiong, H. Liu, L. Yang, Y. Chen and H. Li, *Carbon*, 2022, **197**, 87-97.

48. G. Yin, Y. Wang, W. Wang and D. Yu, *Colloids and Surfaces A: Physicochemical and Engineering Aspects*, 2020, **601**, 125047.

49. G. S. Lee, T. Yun, H. Kim, I. H. Kim, J. Choi, S. H. Lee, H. J. Lee, H. S. Hwang, J. G. Kim and D.-w. Kim, *ACS Nano*, 2020, **14**, 11722-11732.

50. H. Wu, Y. Xie, Y. Ma, B. Zhang, B. Xia, P. Zhang, W. Qian, D. He, X. Zhang and B. W. Li, *Small*, 2022, **18**, 2107087.

51. B. Shen, W. Zhai and W. Zheng, *Adv. Funct. Mater.*, 2014, **24**, 4542-4548.

52. J. Zeng, X. Ji, Y. Ma, Z. Zhang, S. Wang, Z. Ren, C. Zhi and J. Yu, *Adv. Mater.*, 2018, **30**, 1705380.

53. Y. Sun, X. Han, P. Guo, Z. Chai, J. Yue, Y. Su, S. Tan, X. Sun, L. Jiang and L. Heng, *ACS Nano*, 2023.

54. W. L. Song, X. T. Guan, L. Z. Fan, W. Q. Cao, C. Y. Wang, Q. L. Zhao and M. S. Cao, *Journal of Materials Chemistry A*, 2015, **3**, 2097-2107.

55. T. Zhou, C. Xu, H. Liu, Q. Wei, H. Wang, J. Zhang, T. Zhao, Z. Liu, X. Zhang and Y. Zeng, *ACS Nano*, 2020, **14**, 3121-3128.

56. M. Tan, D. Chen, Y. Cheng, H. Sun, G. Chen, S. Dong, G. Zhao, B. Sun, S. Wu and W. Zhang, *Advanced Functional Materials*, 2022, **32**, 2202057.

57. H. Zhang, G. Zhang, M. Tang, L. Zhou, J. Li, X. Fan, X. Shi and J. Qin, *Chem. Eng. J.*, 2018, **353**, 381-393.

58. A. Sheng, W. Ren, Y. Yang, D. X. Yan, H. Duan, G. Zhao, Y. Liu and Z. M. Li, *Compos. - A: Appl. Sci. Manuf.*, 2020, **129**, 105692.

59. F. Sharif, M. Arjmand, A. A. Moud, U. Sundararaj and E. P. Roberts, *ACS Appl. Mater. Interfaces.*, 2017, **9**, 14171-14179.

60. Y. Yang, S. Chen, W. Li, P. Li, J. Ma, B. Li, X. Zhao, Z. Ju, H. Chang and L. Xiao, *ACS Nano*, 2020, **14**, 8754-8765.

61. X. He, L. Feng, Z. Zhang, X. Hou, X. Ye, Q. Song, Y. Yang, G. Suo, L. Zhang and Q. G. Fu, *ACS Nano*, 2021, **15**, 2880-2892.

62. L. Wang, H. Qiu, C. Liang, P. Song, Y. Han, Y. Han, J. Gu, J. Kong, D. Pan and Z. Guo, *Carbon*, 2019, **141**, 506-514.

63. K. Zhang, G. H. Li, L. M. Feng, N. Wang, J. Guo, K. Sun, K. X. Yu, J. B. Zeng, T. Li and Z. Guo, *J. Mater. Chem. C.*, 2017, **5**, 9359-9369.

64. A. Gebrekrstos, S. Biswas, A. V. Menon, G. Madras, P. Pötschke and S. Bose, *Composites Part B: Engineering*, 2019, **166**, 749-757.

65. Z. Zeng, H. Jin, M. Chen, W. Li, L. Zhou, X. Xue and Z. Zhang, *Small*, 2017, **13**, 1701388.

66. C. Fu, Z. Sheng and X. Zhang, *ACS Nano*, 2022.

67. L. C. Jia, Y. K. Li and D. X. Yan, *Carbon*, 2017, **121**, 267-273.

68. Q. Zhou, J. Lyu, G. Wang, M. Robertson, Z. Qiang, B. Sun, C. Ye and M. Zhu, *Adv. Funct. Mater.*, 2021, **31**, 2104536.

69. Z. Ma, X. Xiang, L. Shao, Y. Zhang and J. Gu, *Angewandte Chemie International Edition*, 2022, **61**, e202200705.

70. F. Peng, W. Zhu, Y. Fang, B. Fu, H. Chen, H. Ji, X. Ma, C. Hang and M. Li, *ACS Applied Materials & Interfaces*, 2023, **15**, 4284-4293.

71. H. K. Choi, A. Lee, M. Park, D. S. Lee, S. Bae, S. K. Lee, S. H. Lee, T. Lee and T. W. Kim, *ACS Nano*, 2021, **15**, 829-839.

72. S. Xia, C. Wei, J. Tang and J. Yan, *ACS Sustainable Chemistry & Engineering*, 2021, **9**, 13999-14005.